# Anisotropic resistance switching in hexagonal manganites

Xueyun Wang,[1,*] Danni Yang,[2] Hui-Min Zhang,[3] Chuangye Song,[2] Jing Wang,[2] Guotai Tan,[2] Renkui Zheng,[4]
Shuai Dong,[3,†] Sang-Wook Cheong,[5] and Jinxing Zhang[2,‡]

[1]*School of Aerospace Engineering, Beijing Institute of Technology, Beijing 100081, China*
[2]*Department of Physics, Beijing Normal University, Beijing 100875, China*
[3]*School of Physics, Southeast University, Nanjing 211189, China*
[4]*State Key Laboratory of High Performance Ceramics and Superfine Microstructure,*
*Shanghai Institute of Ceramics, Chinese Academy of Sciences, Shanghai 200050, China*
[5]*Rutgers Center for Emergent Materials and Department of Physics and Astronomy, Rutgers University, Piscataway, New Jersey 08854, USA*

The distribution and manipulation of oxygen defects, including oxygen vacancies ($O_v$) and interstitial oxygen ($O_i$), directly results in modifications in a variety of emergent functionalities in transition metal oxides. This is applicable in nanoscale control, which is a key issue in data and energy storage devices, such as resistive switching memory. Among all the oxygen-defect-related topics, nanoscale oxygen defect migration paths have a direct impact on the performance of memory devices, and are intrinsically determined by the structural anisotropy. Here, we use layered single-crystalline ferroelectric, hexagonal manganites ($h$-REMnO$_3$) to demonstrate $O_i$-migration-induced nanoscale manipulation of conductance in the $ab$ plane. Conversely, this unique phenomenon cannot be achieved along the $c$ axis. Furthermore, a density functional theory calculation reveals that the energy barriers are lower for planar migrations of $O_i$, when compared to out-of-plane migration, and are responsible for such anisotropic resistance switching.

The growing interest in understanding the effects of the distribution and manipulation of defects in functional materials is driven by emerging novel phenomena such as superconductivity [1,2], metal-to-insulator transitions [3], and potential applications including resistive switching memory [4–7] and lithium batteries [8]. In particular, oxygen defects, including oxygen vacancies ($O_v$) and interstitial oxygen ($O_i$), are elemental point defects (which can be considered to be a mobile electron donor and acceptor, respectively) in complex oxides, that play prominent roles in disturbing the ground state and dictating the functional properties of these oxides [9]. Due to variable valences of transition metal elements, oxygen defects naturally exist in oxide-based thin films and crystals, especially in complex transition metal oxides [10]. Numerous efforts have been made to study the emerging functional phenomena triggered by oxygen defects, such as $O_i$-induced superconductivity in the layered superconductor La$_2$CuO$_{4+\delta}$ [1], $O_v$-suppressed metal to insulator transition in VO$_2$ [11], induced ferromagnetism in perovskite SrTiO$_3$ [12], etc. These studies exemplify the role of oxygen defects in tuning the interplay among different degrees of freedom (lattice, charge, and spin), leading to further potential controllability of the crystalline, electronic, and magnetic structures. Furthermore, to pave the path for potential high-density storage applications, the nanoscale manipulation of oxygen defects in the presence of external fields is urgently required.

Recent works have demonstrated that $O_v$ is an effective tunable parameter at the nanoscale, and can lead to fascinating phenomena [13–17]. However, the manipulation of $O_i$ at the nanoscale still remains unexplored. Meanwhile, the migration paths and barrier energies of the oxygen defects are naturally determined by the crystalline anisotropy, which governs the feasibility of controlling oxygen defects in various materials [5,6]. Note that most previous studies focused on the thin films or device-based heterostructures, in which the substrate and interface effects may produce a critical influence on the oxygen defects manipulation. Thus, it is necessary to understand and demonstrate the manipulation of oxygen defects in functional oxides, especially through the intrinsic crystalline anisotropy.

Hexagonal ($h$)-REMnO$_3$($RE$ = rare earths) is a well-studied improper ferroelectric family with the emergence of topological ferroelectric vortices [18,19]. It crystallizes in a hexagonal structure with close-packed layers of MnO$_5$ polyhedra, separated by layers of rare earth ions [20,21], that provide enough space for the formation of oxygen defects, as well as possible anisotropic oxygen defect migration paths (in the $ab$ plane or along the $c$ axis) [15,22–28]. Although ferroelectricity is along the $c$ axis, the ferroelectric domains show a similar sixfold vortex-antivortex pattern on arbitrarily oriented planes [29,30], such as the $ab$ plane (surface with out-of-plane polarized domains) and the $ac$ plane (surface with in-plane polarized domains) shown in Fig. 1(e). By taking advantage of this three-dimensional ferroelectric domain morphology, the anisotropic behaviors can be visualized and manipulated using scanning probe microscopy on different

*xueyun@bit.edu.cn
†sdong@seu.edu.cn
‡jxzhang@bnu.edu.cn
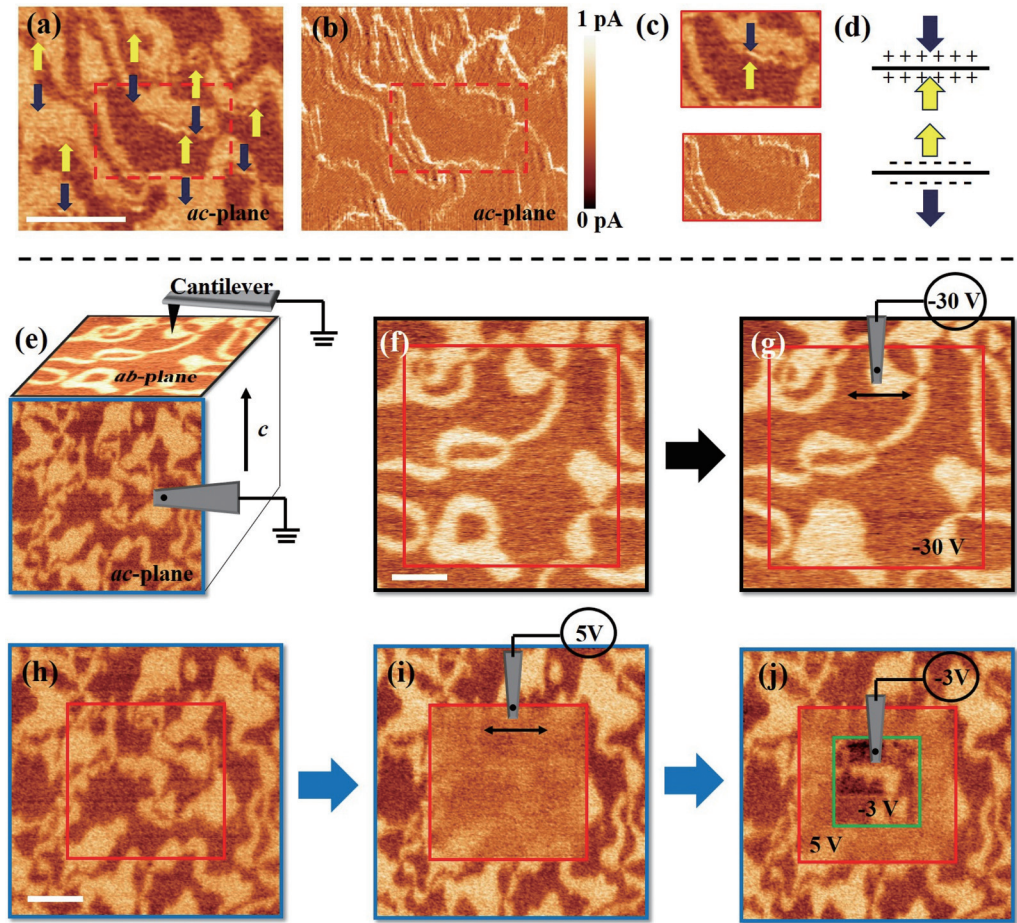
FIG. 1. c-AFM and PFM scanning images. (a,b) display the in-plane PFM and corresponding c-AFM on the *ac* plane. (c) is a comparison between PFM and c-AFM images in the red-boxed region, showing the conductive tail-to-tail domain wall and nonconductive head-to head domain wall. (d) is a schematic showing two types of domain walls. (e) is a collaged three-dimensional image showing topological vortices on both the *ab* plane and the *ac* plane. (f,g) are images on the *ab* plane before and after the application of −30 V tip voltage. Note that the loop domain at the bottom-left corner of the red-boxed region changed into a bubble domain. (h–j) are PFM images on the *ac* plane with no electric field, 5 V on the tip, and −3 V on the tip, consecutively. The red- (green-) boxed region has a positive (negative) voltage applied on the tip. The scale bar is 1 $\mu$m.

orientations of the crystal. Here, we chose *h*-REMnO$_3$ as a model system, combined with piezoresponse force microscopy (PFM), conductive-atomic force microscopy (c-AFM) techniques, x-ray photoelectron spectroscopy (XPS), and scanning tunneling microscopy (STM) to demonstrate the reversible manipulation of conductance perpendicular to the *c* axis, while also showing that this effect is absent along the *c* axis. We propose that this reversible behavior results from easier in-plane O$_i$ diffusion, as opposed to along the *c* axis. This phenomenon is further confirmed by density functional theory (DFT) calculations.

Regarding the dominant type of oxygen defect in *h*-REMnO$_3$, most studies state that the oxygen defect is O$_v$, which can act as a very efficient functional defect for tuning structural, electronic, and magnetic properties, and even to manipulate domain walls [16,22–26,31]. However, recently, Skjærvø *et al.* [28] reported that O$_i$ is responsible for *p*-type conductivity in *h*-REMnO$_3$. Therefore, before the manipulation of oxygen defects, it is crucial to verify the dominant oxygen defect, O$_i$ or O$_v$. Our single-crystalline Y$_{0.67}$Lu$_{0.33}$MnO$_3$ (YLMO) with a cleaved *ab* plane and a

large cut *ac* plane, was grown using the floating zone method followed by a standard furnace cooling. We demonstrate that *p*-type conductivity is dominant by performing PFM and corresponding c-AFM scans, as shown in Figs. 1(a) and 1(b), suggesting O$_i$ as the dominant oxygen defect. On the *ac* plane, the yellow and blue arrows indicate the in-plane polarization directions. An enlarged red-boxed region, as shown in Fig. 1(c), clearly reveals that the tail-to-tail domain walls are conductive. A schematic of the tail-to-tail and head-to-head domain walls is shown in Fig. 1(d) to illustrate that the charged 180° domain walls in ferroelectric semiconductors attract charge carriers with an opposite sign. Therefore, the more conductive tail-to-tail domain walls imply that the dominant carriers are holes (*p*-type conductivity) [32,33]. The results are also consistent with similar experiments for *p*-type ErMnO$_3$ [34] and HoMnO$_3$ [35] single crystals. In addition, XPS and STM experiments on the identical single crystal supports the idea that O$_i$ is the dominating defect (see Supplemental Material [36], Sec. 1, for XPS and STM details; also see [37–48]). There  may be O$_v$ that exist; however, considering the chemical equilibrium, the valence state of
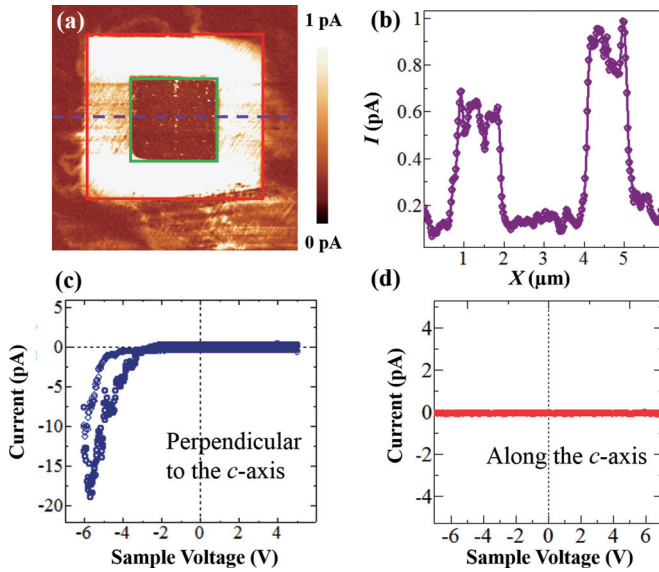
FIG. 2. c-AFM measurement and *I-V* curves. (a) shows the local current measurement over a $5 \times 5 \, \mu m^2$ area after the application of $+4 \, V$ on a $3 \times 3 \, \mu m^2$ area (red square) and sequentially poling with $-4.5 \, V$ on a $1 \times 1 \, \mu m^2$ area (green square). The bright region indicates high current. (b) is the current profile along the purple dashed line. (c,d) are *I-V* curves along two different orientations measured using the c-AFM technique.

Mn ions, and conductive tail-to-tail (insulating head-to-head) domain walls, $O_i$ should be dominant, while $O_v$ should be negligible.

The ferroelectric vortices on both the *ab* plane and the *ac* plane are shown in Fig. 1(e). On the *ab* plane, by sweeping a $4 \times 4 \, \mu m^2$ red-boxed region with a tip voltage of $-30 \, V$, the domain pattern is similar to that before a voltage is applied, except that the loop domain located at the bottom-left corner has been changed into a bubble domain by removing the inner domain wall [49], as shown in Figs. 1(f) and 1(g). On the contrary, on the *ac* plane [the PFM data are shown in Fig. 1(h)], we found surprisingly that a $3 \times 3 \, \mu m^2$ red-boxed region poled with a tip voltage of 5 V exhibits the eradication of ferroelectric vortex domains, and no piezoresponse was detected, as shown in Fig. 1(i). Inside the red-boxed region, a $1.5 \times 1.5 \, \mu m^2$ green-boxed region was subsequently poled downward with a tip voltage of $-3$ V, and the ferroelectric domain was restored with an identical domain pattern, as clearly shown in Fig. 1(j).

To understand the mechanism behind this unique behavior of the ferroelectric domain in YLMO, c-AFM was used to measure the local conductance on the electrically poled regions. In Fig. 2(a), the region poled with a positive tip voltage shows a significantly enhanced conductivity that can be switched back to the original insulating state by applying a negative tip voltage. Note that the poled region is more conductive than the charged domain walls. The c-AFM line profile reveals that the current enhancement is in the pA level for a 300-μm-thick single crystal, as shown in Fig. 2(b). The high-conductance state influences the piezoelectric response, namely, the displacement under an alternating electric field [50], leading to weak or no detection of the ferroelectric order

in hexagonal manganites. When comparing the PFM images for two different crystallographic directions, we found that on the *ab* plane, neither a large positive nor a negative voltage could induce the highly conductive state. This is also consistent with the current (*I*)-voltage (*V*) curve measurements. In the presence of a $-6 \, V$ sample voltage perpendicular to the *c* axis (corresponding to PFM scanning on the *ac* plane), the current increased significantly to 20 pA with a nonlinear feature [see Fig. 2(c)]. The *I-V* curve along the *c* axis exhibits no obvious change within the sample voltage range of $-7 \, V$ to 7 V [see Fig. 2(d)]. Note that the current shows no significant change up to the instrument limitation (10 V). This observed phenomenon is repeatable over the same region as well as other regions of the sample. We would like to emphasize that a negative tip voltage (positive sample voltage) on the *ac* plane produces no significant change in the conductivity. This is due to an asymmetric response caused by a Schottky barrier between the tip and the sample surface [14] (see Supplemental Material [36], Sec. 2, for PFM scanning data with a negative tip voltage).

Regarding the hexagonal layered structure, we propose that the enhanced conductance on the *ac* plane is induced by the migration of $O_i$ manipulated by an external electric field. DFT calculations were performed to study the anisotropic $O_i$ migration energies in hexagonal manganite (see Supplemental Material [36], Sec. 3, for details). First, the DFT structural relaxation of the ferroelectric state of *h*-YMnO₃ leads to $a = 6.13 \, Å$, and $c = 11.39 \, Å$, both of which are within a 0.4% error region when compared with the room temperature experimental data reported in Ref. [51]. Such an excellent agreement provides a solid starting point for the following calculations for $O_i$. Then, one more oxygen is added to a $2 \times 2 \times 1$ supercell (24 Mn ions in total). Thus, the $O_i$
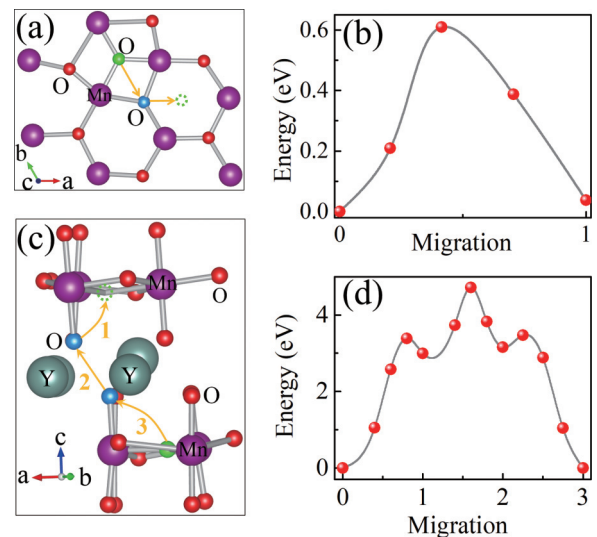


FIG. 3. DFT calculation of oxygen migrations. The oxygen ions involved in the nudging process are highlighted using different colors. (a) The nudging process for in-plane migration, as indicated by arrows. (b) The corresponding migration energy barrier for the in-plane nudging process. (c) The possible out-of-plane nudging path for oxygen migration. (d) The corresponding migration energy barriers for the out-of-plane nudging process, which is much higher than the in-plane one.

concentration can be determined to be ∼1.4%. According to Ref. [28], the most stable position for $O_i$ is in the center of a Mn triangle, as shown in Fig. 3(a).

The migration barriers of $O_i$ were calculated using the climbing-image nudged elastic band (CI-NEB) method [48]. According to Ref. [28], the preferred in-plane migration of $O_i$ can be achieved via the nudging process; i.e., one planar O becomes a new $O_i$ and the original $O_i$ takes its place, as shown in Fig. 3(a). The calculated energy barriers for such an in-plane nudging process is approximately 0.48–0.62 eV (depending on associated parameters) [28] and ∼0.61 eV (ours), as shown in Fig. 3(b). It should be noted that the end state is a little higher in energy than the start one, which was also observed in Ref. [27]. The reason is that there are three energy wells within each Mn triangle. During the DFT relaxation, the interstitial oxygen may randomly choose one well. Thus, the start and end states are slightly different in energy. The agreement between our result and Ref. [28] allows us to further investigate the anisotropic migrations.

The out-of-plane nudging process is even more complicated, involving at least three oxygen ions: $O_i$ and two apical O's ($O_a$). The simplest tentative migration path is shown in Fig. 3(c), forming the $O_i \rightarrow O_a \rightarrow O'_a \rightarrow O'_i$ "reaction" chain. This process can occur synchronously in real materials. However, it is technically challenging to perform a reliable simulation of the synchronous migration of three oxygen ions. Instead, here the separated migration steps, (1) $O'_a \rightarrow O'_i$, (2) $O_a \rightarrow O'_a$, and (3) $O_i \rightarrow O_a$, are calculated, as shown in Fig. 3(c). The energy barrier is ∼4.7 eV [Fig. 3(d)],

which is quite a high value. Thus, at room temperature ($k_B T \sim 0.027$ eV), there is a considerable possibility of $O_i$ migrating in the *ab* plane with the help of thermal excitation and an applied electric field, while out-of-plane migration is much more difficult. This preferred in-plane migration explains the in-plane modulation of the conductance, while this effect is absent along the *c* axis.

Combining the experimental observations and theoretical calculations, we find that $O_i$ is critical for the conductance switching process. In addition, the stability of the conductive state on the *ac* plane was also investigated, as shown in Fig. 4(a), where the PFM images were obtained consecutively with the writing conditions for the red- and green-boxed region being 4 V and −4 V on the tip, respectively. The poled region shows no significant change after 5 h. Figure 4(b) shows *I-V* curves for different locations, where occurrences of clear *I-V* hysteresis are observed. Figure 4(c) presents the repeatability for an identical location by cycling through the full hysteresis. For the conducting state to return to the insulating state, a voltage that is higher than −1.5 V has to be applied. Otherwise, the current still exhibits a high value at a voltage of −2.6 V. Note that the conductive pathways created by the anisotropic $O_i$ migration energy are utilized, and this hysteretic *I-V* shape can potentially be used as a prototype for resistive memory utilizing this unique ferroelectric hexagonal manganite. For instance, two different current states at −2.6 V could represent ON/OFF states, respectively.

Reversible switching between insulating and conducting states in oxides is one of the major potential applications in
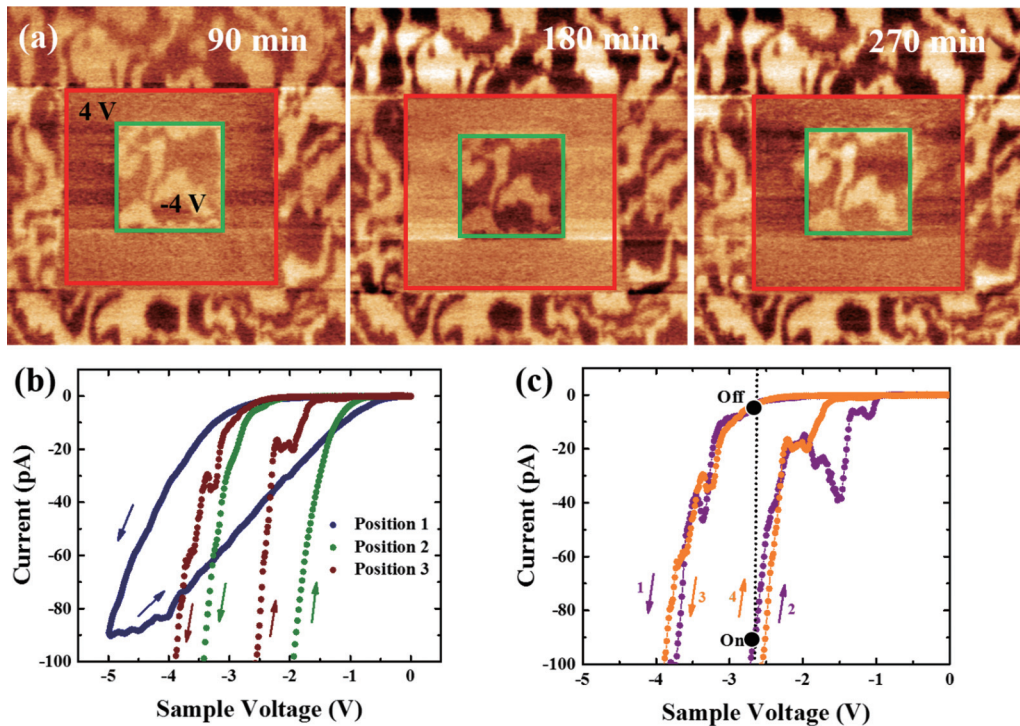


FIG. 4. The stability and repeatability of the conducting state. (a) The writing condition for the red- and green-boxed regions are 4 V and −4 V on the tip, respectively. PFM was performed after writing the box after 90, 180, and 270 min, respectively. (b) shows *I-V* curves of different locations on the *ac* plane. (c) shows a proposed ON/OFF switch at a reading voltage of −2.6 V. The numbers inside the rectangles denote the sequence of voltage sweeps. After returning from +2 V, a high-resistance state at −2.6 V is measured (OFF state), whereas low resistance is obtained (ON state) after returning from −6 V.

memory devices. However, most of the demonstrated examples have been confined to two-dimensional thin films such as Ca-doped $BiFeO_3$ film [14] or isotropic single-crystalline $SrTiO_3$ [3]. In layered hexagonal manganites, through a combined experimental and theoretical approach, we demonstrated controllable bulk conductance using the electrical bias from an scanning probe microscopy tip. The conductance manipulation can be easily achieved along in-plane directions, rather than out-of-plane (along the $c$ axis) directions. This phenomenon can be explained by anisotropic $O_i$ migration energy barriers along different crystallographic directions. $O_i$ preferably migrates following in-plane paths, rather than out-of-plane paths. The oxygen defects also have a strong potential to couple with ferroic orders such as ferroelectricity or long-range magnetic ordering in complex oxides. Thus, the utilization of such intrinsic crystallographic anisotropy and various defects migration paths may also assist in structure design for other point defects with nanoscale controllable properties (e.g., oxygen-defect-induced superconducting states in cuprates and lithium ion migration paths in lithium batteries).

We also propose a prototype of an ON/OFF switch, that takes advantage of this unique manipulation of bulk conductance. This is essential for the development of next-generation oxide-based resistive memory devices.

[1] N. Poccia, M. Fratini, A. Ricci, G. Campi, L. Barba, A. Vittorini-Orgeas, G. Bianconi, G. Aeppli, and A. Bianconi, Nat. Mater. **10**, 733 (2011).

[2] D. J. Werder, C. H. Chen, R. J. Cava, and B. Batlogg, Phys. Rev. B **38**, 5130 (1988).

[3] K. Szot, W. Speier, G. Bihlmayer, and R. Waser, Nat. Mater. **5**, 312 (2006).

[4] R. Waser, R. Dittmann, G. Staikov, and K. Szot, Adv. Mater. **21**, 2632 (2009).

[5] R. Waser and M. Aono, Nat. Mater. **6**, 833 (2007).

[6] W. M. Lu, C. J. Li, L. M. Zheng, J. X. Xiao, W. N. Lin, Q. Li, X. R. Wang, Z. Huang, S. W. Zeng, K. Han, W. X. Zhou, K. Y. Zeng, J. S. Chen, Ariando, W. W. Cao, and T. Venkatesan, Adv. Mater. **29**, 1606165 (2017).

[7] D. Ielmini, Semicond. Sci. Technol. **31**, 063002 (2016).

[8] J. M. Tarascon and M. Armand, Nature **414**, 359 (2001).

[9] H. L. Tuller and S. R. Bishop, Annu. Rev. Mater. Res. **41**, 369 (2011).

[10] S. V. Kalinin and N. A. Spaldin, Science **341**, 858 (2013).

[11] J. Jeong, N. Aetukuri, T. Graf, T. D. Schladt, M. G. Samant, and S. S. P. Parkin, Science **339**, 1402 (2013).

[12] W. D. Rice, P. Ambwani, M. Bombeck, J. D. Thompson, G. Haugstad, C. Leighton, and S. A. Crooker, Nat. Mater. **13**, 481 (2014).

[13] S. Das, B. Wang, Y. Cao, M. R. Cho, Y. J. Shin, S. M. Yang, L. F. Wang, M. Kim, S. V. Kalinin, L. Q. Chen, and T. W. Noh, Nat. Commun. **8**, 615 (2017).

[14] C. H. Yang, J. Seidel, S. Y. Kim, P. B. Rossen, P. Yu, M. Gajek, Y. H. Chu, L. W. Martin, M. B. Holcomb, Q. He, P. Maksymovych, N. Balke, S. V. Kalinin, A. P. Baddorf, S. R. Basu, M. L. Scullin, and R. Ramesh, Nat. Mater. **8**, 485 (2009).

[15] Q. H. Zhang, X. Shen, Y. Yao, Y. G. Wang, C. Q. Jin, and R. C. Yu, J. Alloys Compd. **648**, 253 (2015).

[16] Y. Du, X. L. Wang, D. P. Chen, Y. X. Yu, W. C. Hao, Z. X. Cheng, and S. X. Dou, Phys. Chem. Chem. Phys. **15**, 20010 (2013).

[17] A. Kumar, T. M. Arruda, Y. Kim, I. N. Ivanov, S. Jesse, C. W. Bark, N. C. Bristowe, E. Artacho, P. B. Littlewood, C. B. Eom, and S. V. Kalinin, ACS Nano **6**, 3841 (2012).

[18] T. Choi, Y. Horibe, H. T. Yi, Y. J. Choi, W. D. Wu, and S. W. Cheong, Nat. Mater. **9**, 253 (2010).

[19] S. Artyukhin, K. T. Delaney, N. A. Spaldin, and M. Mostovoy, Nat. Mater. **13**, 42 (2014).

[20] C. J. Fennie and K. M. Rabe, Phys. Rev. B **72**, 100103(R) (2005).

[21] B. B. Van Aken, T. T. M. Palstra, A. Filippetti, and N. A. Spaldin, Nat. Mater. **3**, 164 (2004).

[22] D. P. Chen, Y. Du, X. L. Wang, Z. X. Cheng, S. X. Dou, Z. W. Lin, J. G. Zhu, and B. Xu, J. Appl. Phys. **111**, 07D913 (2012).

[23] S. Cheng, S. Q. Deng, Y. G. Zhao, X. F. Sun, and J. Zhu, Appl. Phys. Lett. **106**, 062905 (2015).

[24] S. Cheng, M. Li, Q. Meng, W. Duan, Y. G. Zhao, X. F. Sun, Y. Zhu, and J. Zhu, Phys. Rev. B **93**, 054409 (2016).

[25] S. B. Cheng, M. L. Li, S. Q. Deng, S. Y. Bao, P. Z. Tang, W. H. Duan, J. Ma, C. W. Nan, and J. Zhu, Adv. Funct. Mater. **26**, 3589 (2016).

[26] Q. H. Zhang, S. D. Guo, B. H. Ge, P. Chen, Y. Yao, L. J. Wang, L. Gu, Y. G. Wang, X. F. Duan, C. Q. Jin, B. G. Liu, and R. C. Yu, J. Am. Ceram. Soc. **97**, 1264 (2014).

[27] S. Remsen and B. Dabrowski, Chem. Mater. **23**, 3818 (2011).

[28] S. H. Skjaervo, E. T. Wefring, S. K. Nesdal, N. H. Gaukas, G. H. Olsen, J. Glaum, T. Tybell, and S. M. Selbach, Nat. Commun. **7**, 13745 (2016).

[29] S. Z. Lin, X. Y. Wang, Y. Kamiya, G. W. Chern, F. Fan, D. Fan, B. Casas, Y. Liu, V. Kiryukhin, W. H. Zurek, C. D. Batista, and S. W. Cheong, Nat. Phys. **10**, 970 (2014).

[30] S. M. Griffin, M. Lilienblum, K. T. Delaney, Y. Kumagai, M. Fiebig, and N. A. Spaldin, Phys. Rev. X **2**, 041022 (2012).

[31] Y. Du, X. L. Wang, D. P. Chen, S. X. Dou, Z. X. Cheng, M. Higgins, G. Wallace, and J. Y. Wang, Appl. Phys. Lett. **99**, 252107 (2011).

[32] M. Y. Gureev, A. K. Tagantsev, and N. Setter, Phys. Rev. B **83**, 184104 (2011).

[33] E. A. Eliseev, A. N. Morozovska, G. S. Svechnikov, V. Gopalan, and V. Y. Shur, Phys. Rev. B **83**, 235313 (2011).

[34] D. Meier, J. Seidel, A. Cano, K. Delaney, Y. Kumagai, M. Mostovoy, N. A. Spaldin, R. Ramesh, and M. Fiebig, Nat. Mater. **11**, 284 (2012).

[35] W. D. Wu, Y. Horibe, N. Lee, S. W. Cheong, and J. R. Guest, Phys. Rev. Lett. **108**, 077203 (2012).

[36] See Supplemental Material at http://link.aps.org/supplemental/10.1103/PhysRevB.99.054106 for XPS, STM, additional PFM data, and DFT details; also see Refs. [28,37–48].

[37] J. F. Moulder, W. F. Stickle, P. E. Sobol, and K. D. Bomben, *Handbook of X-Ray Photoelectron Spectroscopy*, (Perkin-Elmer Corp. Norwalk, CT, 1992).

[38] P. Ren, H. Fan, and X. Wang, Appl. Phys. Lett. **103**, 152905 (2013).

[39] E. T. Yu, M. B. Johnson, and J.-M. Halbout, Appl. Phys. Lett. **61**, 201 (1992).

[40] R. M. Feenstra, E. T. Yu, J. M. Woodall, P. D. Kirchner, C. L. Lin, and G. D. Pettit, Appl. Phys. Lett. **61**, 795 (1992).

[41] G. Kresse and J. Hafner, Phys. Rev. B **47**, 558 (1993).

[42] G. Kresse and J. Furthmüller, Phys. Rev. B **54**, 11169 (1996).

[43] J. P. Perdew, A. Ruzsinszky, G. I. Csonka, O. A. Vydrov, G. E. Scuseria, L. A. Constantin, X. L. Zhou, and K. Burke, Phys. Rev. Lett. **100**, 136406 (2008).

[44] J. P. Perdew, K. Burke, and M. Ernzerhof, Phys. Rev. Lett. **78**, 1396 (1997).

[45] G. Kresse and D. Joubert, Phys. Rev. B **59**, 1758 (1999).

[46] P. E. Blöchl, Phys. Rev. B **50**, 17953 (1994).

[47] S. L. Dudarev, G. A. Botton, S. Y. Savrasov, C. J. Humphreys, and A. P. Sutton, Phys. Rev. B **57**, 1505 (1998).

[48] G. Henkelman, B. P. Uberuaga, and H. Jonsson, J. Chem. Phys. **113**, 9901 (2000).

[49] M. G. Han, Y. M. Zhu, L. J. Wu, T. Aoki, V. Volkov, X. Y. Wang, S. C. Chae, Y. S. Oh, and S. W. Cheong, Adv. Mater. **25**, 2415 (2013).

[50] K. Uchida, S. Tsuneyuki, and T. Schimizu, Phys. Rev. B **68**, 174107 (2003).

[51] G. Nenert, M. Pollet, S. Marinel, G. R. Blake, A. Meetsma, and T. T. M. Palstra, J. Phys.: Condens. Matter **19**, 466212 (2007).